PAPER

Check for updates

The construction of Tb³⁺ doped Sr–BDC metal–organic framework materials and their high-sensitivity fluorescent detection of Fe³⁺

Huan Yang,†[a] Xin Chen,†[a] Yaling Yu,[a] Changjin Liang,[a] Yunying Wu,[a] Boxin Qiu,[a] Chenyang Zhang [ID] *[a] and Shaomin Lin*[ab]

This study presents the synthesis of a strontium-based metal–organic framework (Sr–BDC) through a solvothermal method, employing strontium chloride and terephthalic acid as primary precursors. The as-prepared Sr–BDC was subsequently functionalized with terbium ions (Tb³⁺) to yield a Tb³⁺@Sr–BDC composite. Extensive structural characterization, including X-ray diffraction (XRD), thermogravimetric analysis (TG), and the scanning electron microscope (SEM), confirmed that the Tb³⁺ incorporation preserved the integrity of the Sr-MOF framework without inducing structural degradation. Photoluminescence analysis demonstrated that Tb³⁺@Sr–BDC exhibits distinct Tb³⁺ emission peaks at 545 nm upon excitation at 294 nm, showcasing exceptional selectivity and sensitivity toward Fe³⁺ ions. Stern–Volmer quenching analysis revealed a remarkably low detection limit of 7.3×10^{-6} mol L⁻¹ for Fe³⁺, with a linear response range spanning from 5×10^{-6} to 1×10^{-4} mol L⁻¹. The potential mechanisms responsible for Fe³⁺-induced fluorescence quenching in Tb³⁺@Sr–BDC was also analysised in the study. These results underscore the potential of Tb³⁺@Sr–BDC as a highly efficient fluorescent probe for applications in environmental monitoring and biomedical sensing.

1 Introduction

With the rapid advancements in analytical chemistry and materials science, there is an increasing demand for fluorescent sensing materials with high sensitivity and selectivity.[1,2] This is particularly critical in environmental monitoring and biomedical applications,[3,4] where the detection of metal ions such as iron (Fe³⁺) is of paramount importance.[5,6] Iron ions not only play a vital role in biological systems but are also frequently detected in industrial wastewater and environmental pollutants. Rare-earth metal–organic frameworks (Ln-MOFs) have emerged as a research hotspot in the field of fluorescent sensing[7,8] due to their unique porous structures and tunable chemical functionalities, offering broad application prospects for the detection of cations, anions, small organic molecules, and biomolecules.[9–15]

Metal–organic frameworks (MOFs) possess tunable porosity and abundant active sites, and have demonstrated great potential in electronics,[16] photocatalysis,[17,18] and other fields. Post-synthetic modification (PSM) strategies[19–25] further extend their application in highly sensitive detection. Embedding photoactive Ln³⁺ ions into MOF lattices offers significant advantages:

the intrinsic porosity of the MOF is preserved, while characteristic lanthanide emission—long fluorescence lifetimes, narrow emission bands, and large Stokes shifts—is introduced. Compared with conventional luminescent probes, this approach markedly improves the signal-to-noise ratio and thus detection sensitivity, especially in biological systems with endogenous organic fluorescence. However, the high and variable
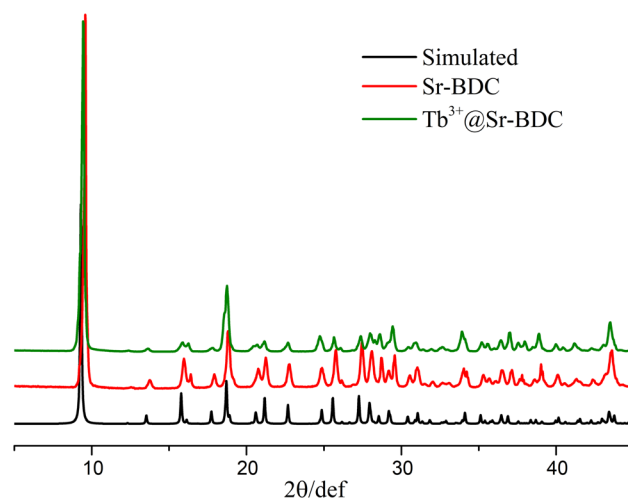

Fig. 1 X-ray powder diffraction (XRD) patterns of Sr–BDC and Tb³⁺@Sr–BDC.

[a] School of Materials Science and Engineering, Hanshan Normal University, Chaozhou, 521041, China. E-mail: zhangchenyang@hstc.edu.cn; lsm678@hstc.edu.cn

[b] Advanced Ceramic Materials Innovation Research Center, Hanshan Normal University, Chaozhou, 521041, China
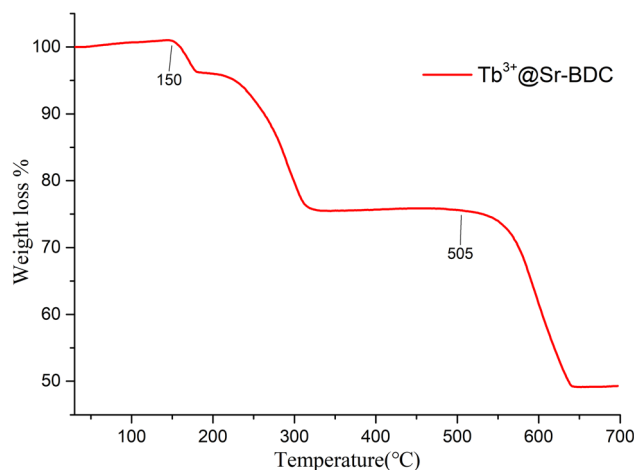
† These authors contributed equally to this work.

Fig. 2   Thermogravimetric analysis (TGA) curve of Tb^{3+}@Sr−BDC.

coordination numbers of rare-earth ions[26] render the direct synthesis of targeted Ln-MOFs challenging. Terbium(III), with its unique electronic configuration and excellent luminescence properties, has been widely used to construct high-performance fluorescent probes. In this work, we employed a post-synthetic modification strategy to embed Tb^{3+} into the Sr−BDC framework, yielding a novel fluorescent probe for the efficient detection of Fe^{3+}.

Among rare-earth ions, terbium (Tb^{3+}) is widely utilized for constructing high-performance fluorescent probes due to its unique electronic configuration and luminescent properties. In

this study, we employed a post-synthetic modification strategy to incorporate Tb^{3+} into the Sr−BDC framework, successfully developing a novel fluorescent probe for the highly efficient detection of Fe^{3+}.

2   Materials and methods

2.1.   Reagents and instruments

Strontium chloride hexahydrate ($SrCl_2 \cdot 6H_2O$), terephthalic acid (H_2BDC), *N,N*-dimethylacetamide (DMA), terbium(III) nitrate hexahydrate ($Tb(NO_3)_3 \cdot 6H_2O$), copper(II) nitrate trihydrate ($Cu(NO_3)_2 \cdot 3H_2O$), chromium(III) nitrate nonahydrate ($Cr(NO_3)_3 \cdot 9H_2O$), nickel(II) nitrate hexahydrate ($Ni(NO_3)_2 \cdot 6H_2O$), iron(III) nitrate nonahydrate ($Fe(NO_3)_3 \cdot 9H_2O$), potassium nitrate (KNO_3), sodium chloride (NaCl), cobalt(II) nitrate ($Co(NO_3)_2$), cadmium(II) nitrate ($Cd(NO_3)_2$), silver nitrate ($AgNO_3$), zinc(II) nitrate hexahydrate ($Zn(NO_3)_2 \cdot 6H_2O$), lead(II) nitrate ($Pb(NO_3)_2$), and absolute ethanol were purchased as analytical-grade reagents and further purified prior to use. All the reagents above were purchased from Macklin.

Thermogravimetric analysis (TGA) was performed using a Netzsch STA 449F3 instrument under a nitrogen atmosphere, with a temperature range of 30–700 °C and a heating rate of 10 °C min^{-1}. X-ray diffraction (XRD) patterns were collected at room temperature using a Rigaku Miniflex 600 diffractometer with Cu Kα radiation ($\lambda = 1.5418$ Å). Fluorescence spectra were recorded at room temperature using a Horiba-HR320 fluorescence spectrophotometer.
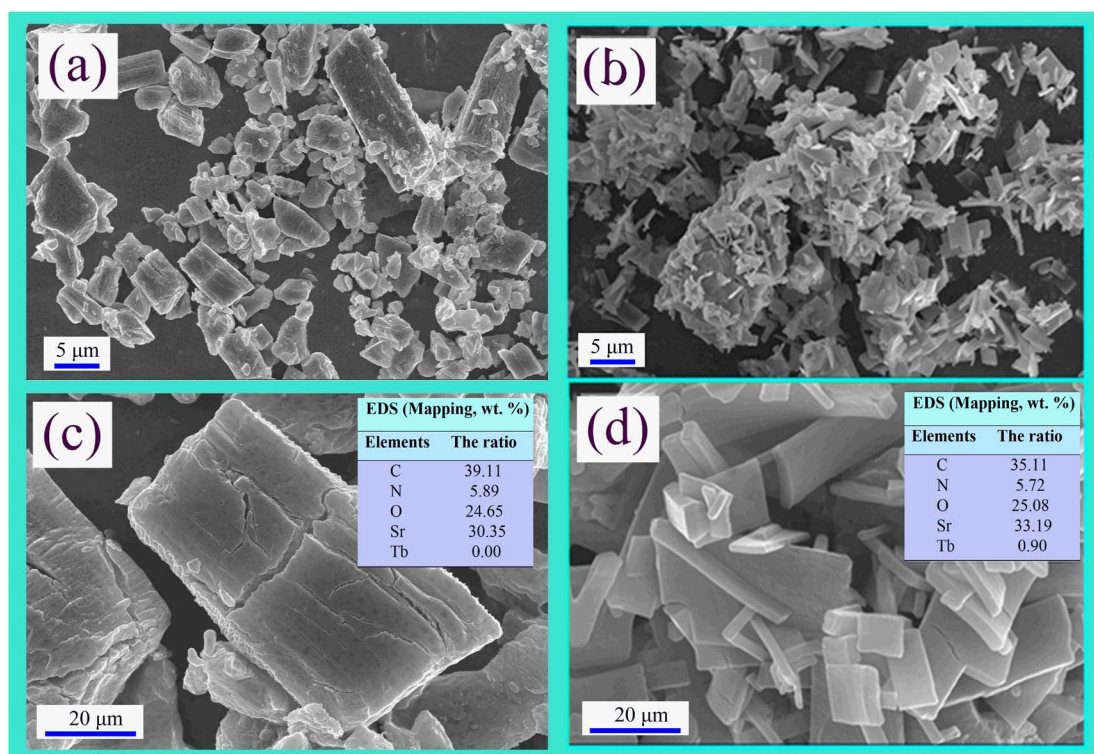

Fig. 3   The SEM images and EDS of the Sr−BDC and Tb^{3+}@Sr−BDC (SEM images: (a) Sr−BDC; (c) Tb^{3+}@Sr−BDC. EDS (mapping): (b) Sr−BDC; (d) Tb^{3+}@Sr−BDC).

The microstructural characterization of the specimens was performed using a Hitachi SU-5000 field-emission scanning electron microscope (FE-SEM, Hitachi High-Tech, Japan) operated at an acceleration voltage of 5–10 kV under high-vacuum conditions. Elemental distribution analysis was conducted *via* energy-dispersive spectroscopy (EDS) utilizing a Bruker Quantax system (Bruker, Germany).

2.2. Synthesis of Sr-BDC and Tb³⁺@Sr-BDC

The systhesis methods and technique were similar with that provided in the previous studies.[27] A mixture of strontium chloride hexahydrate ($SrCl_2 \cdot 6H_2O$, 0.1 mmol, 26.6 mg) and terephthalic acid (H_2BDC, 0.1 mmol, 16.6 mg) was dissolved in 3 mL of *N,N*-dimethylacetamide (DMA). The solution was transferred into a stainless steel autoclave lined with a polytetrafluoroethylene (PTFE) inner tube and heated at 80 °C for 72 h. After the reaction, the autoclave was allowed to cool naturally to room temperature. The resulting colorless block crystals were collected by filtration, washed thoroughly, and dried in air. The final product was weighed for further use.

To prepare Tb³⁺@Sr-BDC, the as-synthesized Sr–BDC powder (100 mg) was immersed in 50 mL of an ethanolic solution of terbium(III) nitrate hexahydrate ($Tb(NO_3)_3 \cdot 6H_2O$), with a $Tb(NO_3)_3$ concentration of 10^{-2} mol L^{-1}, for 24 h. The powder was then separated by centrifugation, washed three times with ethanol, and dried in air for 24 h.

3   Results and discussion

3.1.   The property and structure of the samples

The X-ray powder diffraction (XRD) patterns of Sr–BDC and Tb³⁺@Sr–BDC were recorded at room temperature (Fig. 1). The experimental diffraction peaks of Sr–BDC align well with the simulated pattern (CCDC: 1551141), confirming the synthesis of the Sr–BDC framework. Notably, the diffraction peak positions remain unchanged after Tb³⁺ doping, suggesting that Tb³⁺ ions partially substitute Sr²⁺ sites within the original framework
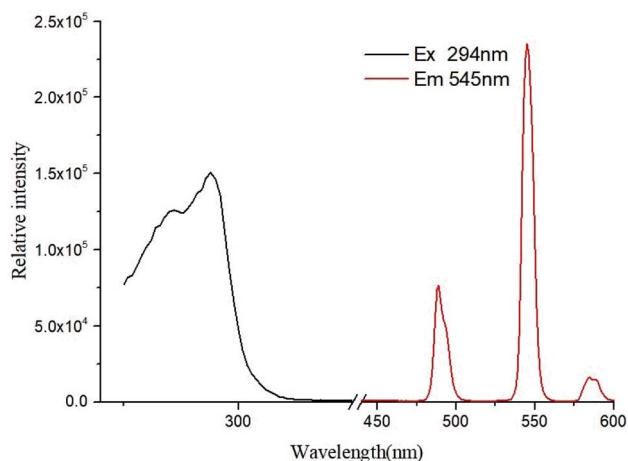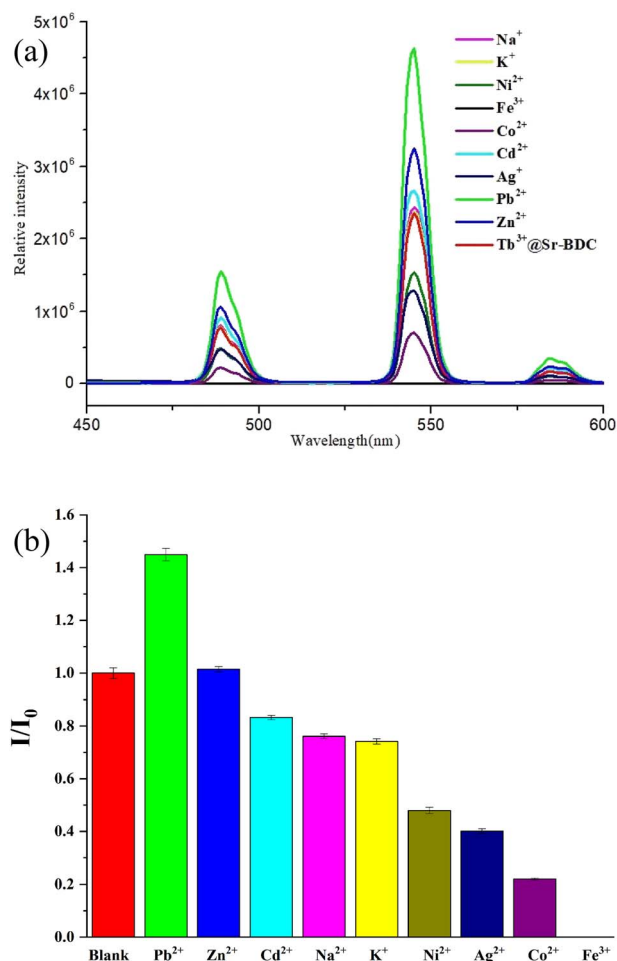

Fig. 5 (a) Emission spectra of Tb³⁺@Sr–BDC in the presence of various metal ions (λ_{ex} = 294 nm) and (b) intensity of the $^5D_4 \rightarrow {}^7F_5$ transition at 545 nm for Tb³⁺@Sr–BDC in the presence of blank (I_0) and the different metal ions solution (I).
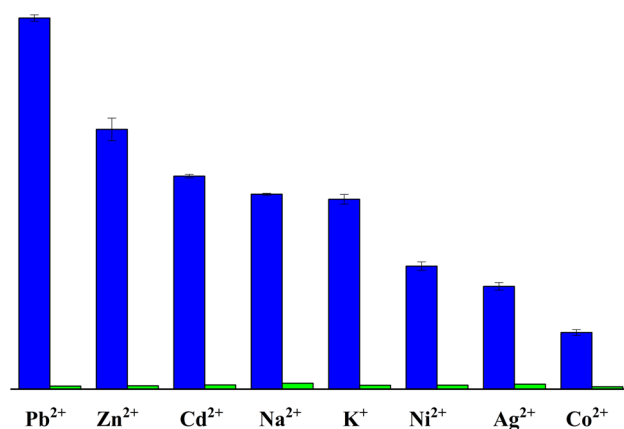

Fig. 6 Intensity of the $^5D_4 \rightarrow {}^7FJ$ transitions for Tb³⁺@Sr–BDC upon addition of different metal ions (1 × 10⁻³ M, blue bars) and subsequent introduction of Fe³⁺ (1 × 10⁻³ M, green bars) (λ_{ex} = 294 nm).

Fig. 4 Excitation (black line) and emission (red line) spectra of Tb³⁺@Sr–BDC.

while preserving its structural integrity. This observation indicates that Tb³⁺@Sr–BDC retains the same crystallographic structure as the parent Sr–BDC.

Thermogravimetric analysis (TGA) of Tb^{3+}@Sr–BDC was conducted in the temperature range of 30–700 °C (Fig. 2). The initial weight loss (150–320 °C) corresponds to the removal of free and coordinated DMA solvent molecules. The Sr–BDC complex (chemical formula: $C_{12}H_{15}NO_6Sr$) exhibited an experimental weight loss of 24.54% within the temperature range of 150–320 °C, demonstrating close agreement with the theoretical mass percentage (24.41%) calculated for the coordinated dimethylacetamide molecule (C_4H_9NO) in its crystal structure. At approximately 505 °C, a structural collapse of the Sr–BDC framework occurs.

Microstructural characterization revealed that Tb^{3+}@Sr–BDC crystals (Fig. 3c and d) exhibited well-faceted short-rod or plate-like morphologies, in contrast to the irregular granular particles observed in undoped Sr–BDC (Fig. 3a and b). Energy-dispersive X-ray spectroscopy (EDS) confirmed the presence of trace Tb (0.90 wt%, Fig. 3d) in Tb^{3+}@Sr–BDC, while no detectable terbium signal was observed in Sr–BDC. These results demonstrate successful Tb^{3+} incorporation into the crystal lattice, which significantly modified the crystallization kinetics and consequently altered the morphological evolution of the crystals.
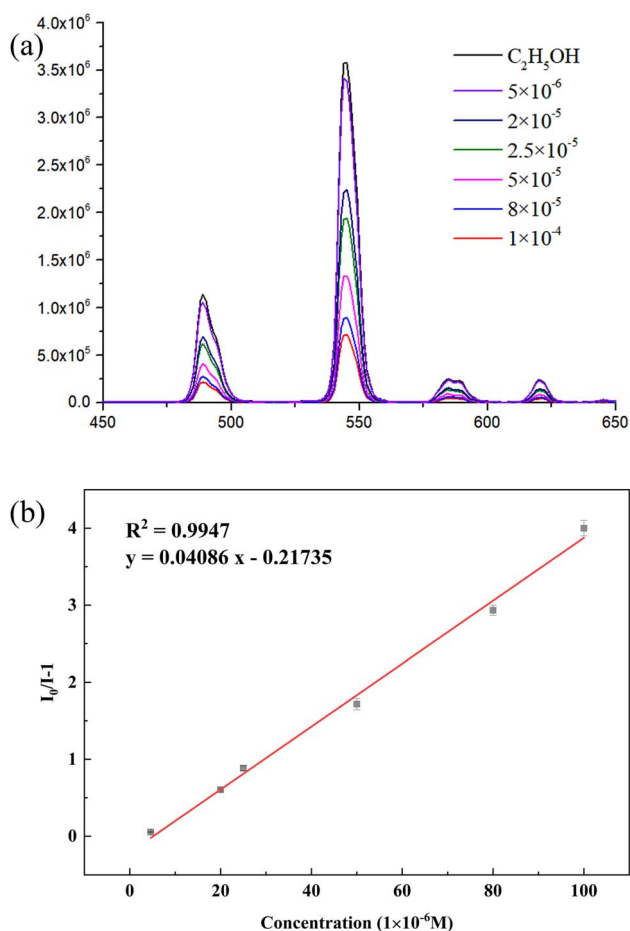
3.2. Luminescence properties of Tb^{3+}@Sr–BDC

As illustrated in Fig. 4, the Tb^{3+}@Sr–BDC material exhibits characteristic emission peaks of Tb^{3+} ions at 489 nm, 545 nm, and 583 nm under 294 nm excitation. These peaks are attributed to the electronic transitions of $^5D_4 \rightarrow {}^7FJ$ ($J = 6, 5, 4$) within Tb^{3+} ions. Notably, the intense green emission at 545 nm suggests that this material can serve as an efficient luminescent sensor.

To evaluate the fluorescence sensing capability of Tb^{3+}@Sr–BDC, its luminescent properties were investigated in the presence of various metal cations. The Tb^{3+}@Sr–BDC powder was finely ground and dispersed in ethanol to form a 5 mg mL^{-1} suspension. Subsequently, 200 μL of the suspension was uniformly mixed with 3.8 mL of ethanol solutions containing 0.001 mol L^{-1} of $M(NO_3)_x$ (M = Pb^{2+}, Zn^{2+}, Cd^{2+}, Na^+, K^+, Ni^{2+}, Ag^+, Co^{2+}, and Fe^{3+}). The luminescence spectra were recorded and are presented in Fig. 5. The results reveal that the luminescence intensity of Tb^{3+} ions is significantly influenced by the presence of different metal ions. The ratio (I/I_0) of the fluorescence intensity at 545 nm for the sample after metal ion introduction (I) to the Tb^{3+}@Sr–BDC sample (I_0) was shown in Fig. 5b. The results suggests that Fe^{3+} induces pronounced luminescence quenching of Tb^{3+}@Sr–BDC, indicating its selective response to Fe^{3+}.

To further investigate the selectivity of Tb^{3+}@Sr–BDC for Fe^{3+}, the material was dispersed in ethanol solutions containing Fe^{3+} alongside other metal ions (Pb^{2+}, Zn^{2+}, Cd^{2+}, Na^+, K^+, Ni^{2+},

Table 1 Comparison of Fe^{3+} ion detection based on different MOF materials

MOF	LOD/(mol L^{-1})	Ref.
[Tb(BTB)(DMF)]	10×10^{-6}	1
[Zn$_2$(tpt)(tda)$_2$]·H$_2$O	4.72×10^{-6}	29
Eu^{3+}@UiO-66	12.5×10^{-6}	30
Zn-MOF-74	1.04×10^{-6}	31
Tb(3+)@Zn-MOF	7.5×10^{-6}	32
Tb^{3+}@Sr-BDC	7.3×10^{-6}	This work

Fig. 7 (a) Emission spectra of Tb^{3+}@Sr–BDC in ethanol solutions with varying Fe^{3+} concentrations (λ_{ex} = 294 nm) and (b) linear relationship between the luminescence intensity of Tb^{3+} and Fe^{3+} concentration in the range of 1×10^{-4} to 5×10^{-6} mol L^{-1}.
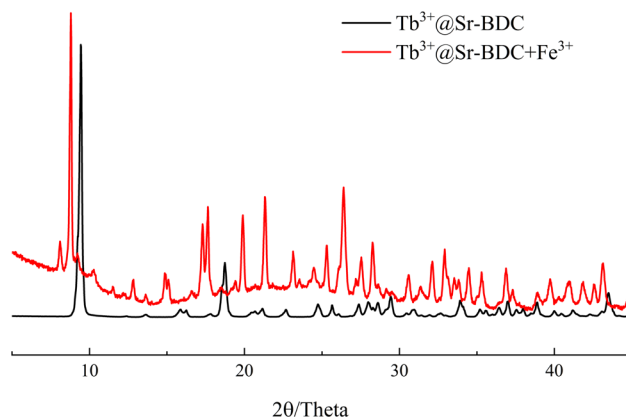
Fig. 8 XRD patterns of Tb^{3+}@Sr–BDC before and after treatment with iron ions.
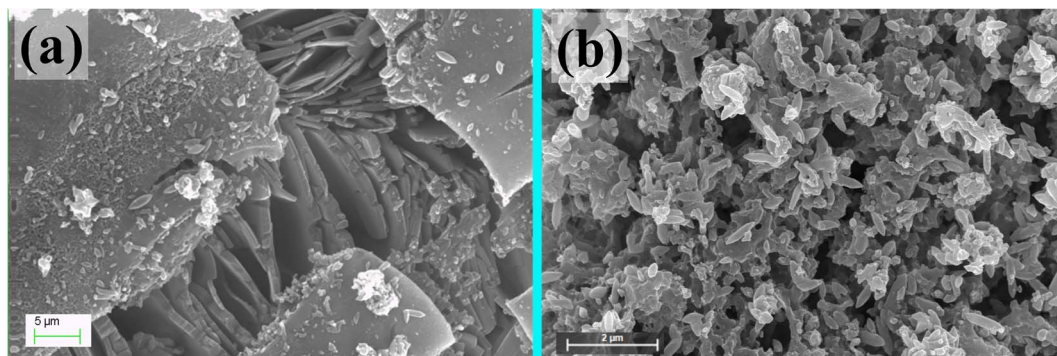
Fig. 9 SEM images of Tb^{3+}@Sr–BDC after treatment with Fe^{3+} at the microscopic scale.

Ag^+, and Co^{2+}). Under 294 nm excitation, the luminescence intensity of Tb^{3+}@Sr–BDC in the presence of individual metal ions (blue bars in Fig. 6) differs significantly from that in mixed-ion solutions containing Fe^{3+} (green bars in Fig. 6). When Tb^{3+}@Sr–BDC is immersed in ethanol solutions containing a mixture of 1×10^{-3} mol L^{-1} of other metal ions and 1×10^{-3} mol L^{-1} of Fe^{3+}, complete luminescence quenching is observed, demonstrating the material's selective detection capability for Fe^{3+} in complex environments.

To quantify the Fe^{3+} detection performance, a concentration gradient of Fe^{3+} solutions was prepared (1×10^{-4} mol L^{-1}, 2×10^{-5} mol L^{-1}, 2.5×10^{-5} mol L^{-1}, 5×10^{-5} mol L^{-1}, 8×10^{-5} mol L^{-1}, and 5×10^{-6} mol L^{-1}). A 0.2 mL aliquot of the 5 mg per mL Tb^{3+}@Sr–BDC–DMA suspension was mixed with 3.8 mL of each Fe^{3+} solution, and the luminescence intensity was measured using a fluorescence spectrophotometer (Fig. 7). The results demonstrate a well-defined linear relationship between Fe^{3+} concentration and the luminescence intensity of Tb@Sr-BDC, with the emission intensity decreasing progressively as Fe^{3+} concentration increases from 5×10^{-6} to 1×10^{-4} mol L^{-1}. Stern–Volmer analysis of the Tb@Sr-BDC + Fe^{3+} system reveals a strong quenching effect, exhibiting a linear correlation coefficient (R) of 0.9947. The limit of detection (LOD = $3\delta/S$, δ represents the blank solution was measured ten times, and S stands for the slope of the calibration curve) was about 7.3×10^{-6} mol L^{-1}.[28] Compared with the reported literature (Table 1), the Tb^{3+}@Sr-BDC sensor exhibits a markedly lower detection limit. These findings confirm that Tb@Sr-BDC not only enables qualitative identification but also facilitates quantitative detection of Fe^{3+} ions.

3.3. Quenching mechanism

The luminescence quenching mechanisms of cations can be attributed to four primary factors:[33,34] (1) interactions between target metal ions and MOFs; (2) exchange between lanthanide ions in MOFs and central metal ions; (3) collapse of the crystalline structure; (4) energy competition between linkers and cations. To elucidate the potential sensing mechanism of Fe^{3+}-induced quenching in Tb^{3+}@Sr–BDC, comprehensive characterization was performed using XRD, SEM, and EDS before and after Fe^{3+} treatment. XRD patterns (Fig. 8) revealed distinct differences between Fe^{3+}-treated and untreated Tb^{3+}@Sr–BDC, indicating framework modification. SEM showed significant morphological alterations in the powdered samples (Fig. 3 and 9). EDS data (Table 2) confirmed the replacement of Tb^{3+} by Fe^{3+} in the framework. The quenching effect is likely caused by displacement of luminescent Tb^{3+} ions by Fe^{3+} and the concurrent framework collapse. This aligns with known cation-MOF interaction paradigms, where heavy metal ions disrupt lanthanide-centered emission through structural and electronic perturbations.

4 Conclusions

A strontium-based metal–organic framework (Sr-MOF) was synthesized *via* a solvothermal reaction using terephthalic acid (H_2BDC) and strontium chloride ($SrCl_2$) as precursors. The as-prepared Sr-BDC was further functionalized with terbium ions (Tb^{3+}) to yield Tb^{3+}@Sr–BDC, which exhibited excellent luminescent properties. Fluorescence sensing studies revealed that Tb^{3+}@Sr–BDC demonstrates high sensitivity and selectivity toward Fe^{3+} ions, with a distinct linear correlation ($R^2 > 0.99$) between fluorescence intensity and Fe^{3+} concentration. The detection limit was determined to be approximately 7.3×10^{-6} mol L^{-1}. These findings highlight the potential of rare-earth-functionalized Sr–BDC materials as efficient fluorescent probes for the detection and quantification of Fe^{3+} in environmental and biomedical applications.

Author contributions

Drafting and the manuscript, H. Y.; investigation, H. Y. and Y. Y.; analysis and interpretation of the data, C. X. and Y. W.; formal analysis, B. Q.; writing-review and editing, C. Z. and S. L.; conception and planning of the work, C. L.

Table 2 Elemental composition analysis (wt%) of Tb^{3+}@Sr–BDC before and after Fe^{3+} coordination (EDS)

Elements	Sr^{2+}	Tb^{3+}	Fe^{3+}
Tb^{3+}@Sr–BDC	33.19	0.90	0
Tb^{3+}@Sr–BDC + Fe^{3+}	32.47	0	3.47

Conflicts of interest

There are no conflicts to declare.

Data availability

The data presented in this study are available on request.

Acknowledgements

References

1 Y. Tang, Y. Li, C. He, *et al.*, NIR-II-Excited Off-On-Off Fluorescent Nanoprobes for Sensitive Molecular Imaging In Vivo, *Nat. Commun.*, 2025, **16**, 278.

2 M. Xing, Y. Han, Y. Zhu, Y. Sun, Y. Shan, K.-N. Wang, Q. Liu, B. Dong, D. Cao and W. Lin, Two Ratiometric Fluorescent Probes Based on the Hydroxyl Coumarin Chalcone Unit with Large Fluorescent Peak Shift for the Detection of Hydrazine in Living Cells, *Anal. Chem.*, 2022, **94**, 12836–12844.

3 X. Fang, S. Wang, Q. Wang, J. Gong, L. Li, H. Lu, P. Xue, Z. Ren and X. Wang, A Highly Selective and Sensitive Fluorescence Probe Based on BODIPY-Cyclen for Hydrogen Sulfide Detection in Living Cells and Serum, *Talanta*, 2024, **268**, 125339.

4 J. Yu, T. Jiang, Z. Lin, H. Yu, S. Wang and Y. Qi, Two Novel Pyrene-Based Schiff Base Fluorescent Probes for the Turn-On Detection of Zn^{2+} and Their Application in Bioimaging, *Microchem. J.*, 2025, **209**, 112715.

5 S. N. Suo, Y. Tian, W. L. Tan, *et al.*, A Near-Infrared Colorimetric Fluorescent Probe for Ferrous Ion Detection and Imaging, *J. Fluoresc.*, 2024, **34**, 1545–1550.

6 C. Y. Zuo, Q. Q. Li, M. Z. Dai, C. Y. Fan, Y. Xu, G. Z. Liu and S. Y. Wang, A Cadmium-Based Metal-Organic Framework for Fluorescent Detection of Acetone and Fe^{3+}, *Chin. J. Inorg. Chem.*, 2023, **39**, 2301–2310.

7 Z. Han, K. Wang, H. C. Zhou, *et al.*, Preparation and Quantitative Analysis of Multicenter Luminescence Materials for Sensing Function, *Nat. Protoc.*, 2023, **18**, 1621–1640.

8 J. Chen, M. Li, R. Sun, Y. Xie, J. R. Reimers and L. Sun, Enhancement of Luminescence from Lanthanide Metal-Organic Frameworks by Ytterbium and Calcium Doping: Application to Photonic Barcodes and Fingerprint Detection, *Adv. Funct. Mater.*, 2024, **34**, 2315276.

9 X. Liu, J. Song, X. Zhang, S. Huang, B. Zhao and X. Feng, A Highly Selective and Sensitive Europium-Organic Framework Sensor for the Fluorescence Detection of Fipronil in Tea, *Food Chem.*, 2023, **413**, 135639.

10 W. P. Lustig, S. Mukherjee, N. D. Rudd, A. V. Desai, J. Li and S. K. Ghosh, Metal–Organic Frameworks: Functional Luminescent and Photonic Materials for Sensing Applications, *Chem. Soc. Rev.*, 2017, **46**, 3242–3285.

11 Z. S. Dou, J. C. Yu, Y. J. Cui, Y. Yu, Z. Y. Wang, D. R. Yang and G. D. Qian, Luminescent Metal-Organic Framework Films as Highly Sensitive and Fast-Response Oxygen Sensors, *J. Am. Chem. Soc.*, 2014, **136**, 5527–5530.

12 S. Y. Wu, Y. Lin, J. Liu, W. Shi, G. Yang and P. Cheng, Rapid Detection of the Biomarkers for Carcinoid Tumors by a Water-Stable Luminescent Lanthanide Metal–Organic Framework Sensor, *Adv. Funct. Mater.*, 2018, **28**, 1707169.

13 B. Li, H. M. Wen, Y. J. Cui, G. D. Qian and B. L. Chen, Multifunctional Lanthanide Coordination Polymers, *Prog. Polym. Sci.*, 2015, **48**, 40–84.

14 S. Y. Zhang, W. Shi, P. Cheng and M. J. Zaworotko, A Mixed-Crystal Lanthanide Zeolite-like Metal–Organic Framework as a Fluorescent Indicator for Lysophosphatidic Acid, a Cancer Biomarker, *J. Am. Chem. Soc.*, 2015, **137**, 12203–12206.

15 C. Chen, X. Wang, L. Li, Y. Huang and R. Cao, Highly selective sensing of Fe3+ by an anionic metal-organic framework containing uncoordinated nitrogen and carboxylate oxygen sites, *Dalton Trans.*, 2018, **47**(10), 3452–3458.

16 Z. Jing, D. Si, H. Guo, L. Han, R. Cao and Y. Huang, Boosting CO_2 Electroreduction by Preactivation Strategy over Carbene-Based Meta-Organic Framework, *CCS Chem.*, 2024, **6**, 3053–3064.

17 X. Li, X. Feng, D. Meng, X. Hu, L. Li, Y. Zhang and X. Wang, Fabrication of TiO_2/MOF Type II Heterojunction by Growth of TiO_2 on Cr-Based MOF for Enhanced Photocatalytic Hydrogen Production, *Cryst. Growth Des.*, 2025, **25**(4), 1182–1189.

18 H. Zhao, J. Liu, S. Chang, Z. Meng, X. Wang and H. Gao, Triple Biomimetic Surfaces with Patterned Anisotropic Wettability for Multiscale Droplets Manipulation, *Nano Lett.*, 2025, **25**(14), 5638–5645.

19 Y. Zhang and B. Yan, A Point-of-Care Diagnostics Logic Detector Based on Glucose Oxidase Immobilized Lanthanide Functionalized Metal-Organic Frameworks, *Nanoscale*, 2019, **11**, 22946–22953.

20 Y. Zhang and B. Yan, MIL-61 and Eu^{3+}@MIL-61 as Signal Transducers to Construct an Intelligent Boolean Logical Library Based on Visualized Luminescent Metal-Organic Frameworks, *ACS Appl. Mater. Interfaces*, 2019, **11**, 21025–21033.

21 J. M. Zhou, H. H. Li, H. Zhang, H. M. Li, W. Shi and P. Cheng, A Bimetallic Lanthanide Metal-Organic Material as a Self-Calibrating Color-Gradient Luminescent Sensor, *Adv. Mater.*, 2015, **27**, 7072–7077.

22 Y. Z. Huang, L. Li, Y. Zhang, L. N. Zhang, S. G. Ge, H. Li and J. H. Yu, Cerium Dioxide-Mediated Signal "On–Off" by Resonance Energy Transfer on a Lab-On-Paper Device for Ultrasensitive Detection of Lead Ions, *ACS Appl. Mater. Interfaces*, 2017, **9**, 32591–32598.

23 B. Yan, Lanthanide Functionalized Metal-Organic Frameworks Hybrid Systems to Create Multiple Luminescent Centers for Chemical Sensing, *Acc. Chem. Res.*, 2017, **50**, 2789–2798.

24 J. F. Feng, S. Y. Gao, T. F. Liu, J. L. Shi and R. Cao, Preparation of Dual-Emitting Ln@UiO-66-Hybrid Films via Electrophoretic Deposition for Ratiometric Temperature Sensing, *ACS Appl. Mater. Interfaces*, 2018, **10**, 6014–6023.

25 Y. Wang, F. Zhang, Z. S. Fang, M. H. Yu, Y. Y. Yang and K. L. Wong, The Tb(III) Postsynthetic Functional Coordination Polymer Coatings on ZnO Micronano Arrays and Application in Small Molecule Sensing, *J. Mater. Chem. C*, 2016, **4**, 8466–8472.

26 C. J. Xu and W. Zhou, Research Progress on Photoluminescent Hybrid Materials Based on Rare Earth Complexes, *J. Rare Earths*, 2015, **33**, 513–523.

27 Y. Wang, S. Lin, L. Jun, R. Huang, H. Cai, W. Yan and H. Yang, A Novel Tb@Sr-MOF as Self-Calibrating Luminescent Sensor for Nutritional Antioxidant, *Nanomaterials*, 2018, **8**, 796.

28 Y. He, H. Zou, X. Jiang, Y. Wei, S. Li, T. Wu and Z. Zhang, A smartphone-assisted fluorescent sensor using Eu/Tb-MOF nanorods for ultrasensitive and visual monitoring of carbendazim in food samples, *Microchem. J.*, 2025, **209**, 112602.

29 X. R. Zhuang, X. Zhang, N. X. Zhang, Y. Wang, L. Y. Zhao and Q. F. Yang, Novel multifunctional Zn metal-organic framework fluorescent probe demonstrating unique sensitivity and selectivity for detection of PA and Fe^{3+} ions in water solution, *Cryst. Growth Des.*, 2019, **19**(10), 5729–5736.

30 L. N. Li, S. S. Shen, W. P. Ai, S. Y. Song, Y. Bai and H. W. Liu, Facilely synthesized Eu3+ post-functionalized UiO-66-type metal-organic frame-work for rapid and highly selective detection of Fe3+ in aqueous solution, *Sens. Actuators, B*, 2018, **267**, 542–548.

31 J. Wang, Y. Fan, H. Lee, C. Yi, X. Zhao and M. Yang, Ultrasmall metal-organic framework Zn-MOF-74 nanodots: size-controlled synthesis and application for highly selective colorimetric sensing of Ironîin aqueous solution, *ACS Appl. Nano Mater.*, 2018, **1**(7), 3747–3753.

32 Y. Wang, R. Huang, J. Zhang, G. Cheng and H. Yang, Lanthanide (Tb^{3+}, Eu^{3+})-functionalized a new one dimensional Zn-MOF composite as luminescent probe for highly selectively sensing Fe^{3+}, *Polyhedron*, 2018, **148**, 178–183.

33 Y.-Y. Liang, L.-J. Luo, Y. Li, B.-K. Ling, B.-W. Chen, X.-W. Wang and T.-G. Luan, Europium(III)-Functionalized Strontium-Based Metal-Organic Framework as a Fluorescent Probe for the Detection of 2,4,6-Trinitrophenol, *Eur. J. Inorg. Chem.*, 2019, **2019**(2), 206–213.

34 H. Yang, C. Zhou, Y. Yang, Z. Chu, W. Yan, S. Nie, J. Luo, S. Lin and Y. Wang, A New Three-Sensing-Channels Platform of Europium(III)-Doped Zinc(II) Metal-Organic Framework for Quantitative Detection of Chromium(III), *Inorg. Chem. Commun.*, 2020, **116**, 107893.